

# An MR-Conditional High-Torque Pneumatic Stepper Motor for MRI-Guided and Robot-Assisted Intervention

YUE CHEN,<sup>1</sup> KA-WAI KWOK,<sup>1,2,3</sup> and ZION Tsz Ho Tse<sup>1</sup>

<sup>1</sup>College of Engineering, The University of Georgia, Athens, GA, USA; <sup>2</sup>Brigham and Women's Hospital, Harvard Medical School, Boston, MA, USA; and <sup>3</sup>Department of Mechanical Engineering, The University of Hong Kong, Hong Kong, China

(Received 9 March 2014; accepted 29 May 2014; published online 24 June 2014)

Associate Editor Agata A. Exner oversaw the review of this article.

**Abstract**—Magnetic resonance imaging allows for visualizing detailed pathological and morphological changes of soft tissue. MR-conditional actuations have been widely investigated for development of image-guided and robot-assisted surgical devices under the Magnetic resonance imaging (MRI). This paper presents a simple design of MR-conditional stepper motor which can provide precise and high-torque actuation without adversely affecting the MR image quality. This stepper motor consists of two MR-conditional pneumatic cylinders and the corresponding supporting structures. Alternating the pressurized air can drive the motor to rotate each step in 3.6° with the motor coupled to a planetary gearbox. Experimental studies were conducted to validate its dynamics performance. Maximum 800 mN m output torque is achieved. The motor accuracy independently varied by two factors: motor operating speed and step size, was also investigated. The motor was tested within a 3T Siemens MRI scanner (MAGNETOM Skyra, Siemens Medical Solutions, Erlangen, Germany) and a 3T GE MRI scanner (GE SignaHDx, GE Healthcare, Milwaukee, WI, USA). The image artifact and the signal-to-noise ratio (SNR) were evaluated for study of its MRI compliancy. The results show that the presented pneumatic stepper motor generated 2.35% SNR reduction in MR images. No observable artifact was presented besides the motor body itself. The proposed motor test also demonstrates a standard to evaluate the pneumatic motor capability for later incorporation with motorized devices used under MRI.

**Keywords**—MRI, Pneumatic stepper motor, MR-conditional.

## INTRODUCTION

Magnetic resonance imaging (MRI) is a non-invasive imaging approach to acquire high-resolution images of soft tissue, not just in the paradigm of

preoperative diagnosis,<sup>21</sup> but also intraoperative therapy.<sup>13</sup> The MR image acquisition does not induce any ionizing radiation which is found in X-ray and CT. It also provides high quality images of soft tissue without any dose of harmful contrast agents required for other imaging modalities, such as X-ray and positron emission tomography. MRI is capable of detecting subtle pathological and morphological changes in the target of interest, thus attracting much research attention on development of MRI-guided interventions, such as for cardiac electrophysiology (EP) therapy,<sup>6,16</sup> breast biopsy,<sup>18</sup> neurosurgery,<sup>12</sup> and prostate intervention.<sup>9</sup> These surgical procedures couple with increasing demands on designing MR-conditional devices that can provide precise actuation to pinpoint the surgical target; however, the use of ferromagnetic or paramagnetic materials is precluded in MR room. Not only is it because of the safety issue due to the strong magnetic force generated by the scanner, but also these materials are prone to induce their own magnetic flux that distorts the homogeneity of the static and gradient magnetic fields in MRI scanner, thus deteriorating the image quality. Traditional actuation units, such as direct current electric motor, cannot be introduced into the vicinity of the magnet for the reason of MR-safety and image quality. The design of MR-conditional actuation component poses paramount impact on advancing the robot-assisted intervention under MRI.

The MR-conditional actuation approaches can be classified into three categories by taking account of its MR safety and electromagnetic compliance<sup>10</sup>: (1) intrinsically MR-conditional actuators (e.g., mechanical, pneumatic andhydraulic actuators); (2) electric actuators (e.g., piezoelectric and ultrasonic motors); and (3) electromagnetic (EM) actuators (e.g., MR-powered actuators). Electric actuators are power-efficient because of its direct conversion from electric

Address correspondence to Ka-Wai Kwok, Department of Mechanical Engineering, The University of Hong Kong, Hong Kong, China. Electronic mail: kwokkw@hku.edu  
Yue Chen and Ka-Wai Kwok: joint first author.

energy into mechanical energy. Among electric actuators, piezoelectric crystals are inherently MR-conditional, but electric current driving the electric actuators inevitably produce heat, induce EM interferences (EMI), and yield noise in the electronic signals, thus severely reducing the SNR<sup>20</sup> in the MR images. MR safety issues of such actuators require proper location and shielding inside the MR room. EM actuators equipped with permanent magnets have to be shielded and also placed at a safe distance from scanner. Proper shielding of EM actuators makes the implementation very challenging. Safe distance of its placement to MR scanner also hampers its use under many clinical settings. Dupont and co-authors<sup>31</sup> recently developed an EM actuator that utilizes the static magnetic field of the scanner to generate mechanical energy; however, same as the other EM actuators, the scanner magnetic field can still affect the steady performance of the electromagnetic motor itself.<sup>8</sup> These disadvantages have naturally shifted the research focuses towards intrinsically MR-conditional actuations, especially pneumatic approach which demonstrates a couple of advantages over the electric and EM actuations. The energy source of pneumatic actuators—the pressured air supply, is commonly available in MRI rooms. The components used to regulate the air supply are readily MR-conditional. Compared to hydraulic actuators, the risk management of using pneumatic actuator is easier, even in any undesired situation when air leakage takes place inside the MRI scanner. The supply air itself is guaranteed not to interfere with the MR imaging physics.<sup>10</sup> As a result, pneumatic actuators can provide minimal SNR reduction in MR images. These advantages boost much research interest in development of such pneumatic actuation components for MR-compatible intervention devices.<sup>4</sup>

To provide precise actuations or manipulations of the pneumatic MR-conditional motors during MRI-guided treatments, such as needle biopsy<sup>29</sup> or brachytherapy,<sup>9</sup> specific PID control<sup>2</sup> and sliding mode control<sup>32</sup> approaches were recently proposed; however, the extra components, such as sensors and encoders, are the pre-requisite for closing the position feedback loop. In contrast, stepper actuator can operate and move discretely step-by-step without having to incorporate with feedback sensors or encoders, thus achieving controllable precision required for different specifications. To our knowledge, only three pneumatic stepper motors compliant with MR environment have hitherto been proposed. *PneuStep* developed by Stoianovici *et al.*<sup>28</sup> is a stepper motor capable of driving a gear with three diaphragm mechanisms. Another stepper motor proposed by Masamune and co-authors<sup>26</sup> is driven by compressing one of the three pistons against the gears at a time. This motor is smaller in size and

less mechanically complex than *PneuStep*. The authors, Chen *et al.*,<sup>7</sup> recently developed the smallest pneumatic stepper motor among these three motors with the diameter lowered to 10 mm. This motor utilizes two push rods and realizes the unidirectional rotation. All in all, these state-of-the-art stepper motors rely on the intermeshing interaction of different sets of gear teeth to trigger the rotation and stepwise effect, which require precise manufacturing and complex design.

In this paper, we propose a new design simplifying the working principle of conventional pneumatic stepper motor. The motor unit is easily assembled, of low cost (<US\$10) and is designed to be disposable so as to avoid complication of surgical sterilization. The motor composes of two cylinders and supporting structure which are manufactured of materials that do not induce EMI. The entire prototype is very lightweight, 80 g only. It can generate the output torque up to 800 mN m. Each rotation step is minimized to 3.6°. Its working principle, kinematics model, implementation and MR compliance evaluation are discussed with the aim to introduce a design standard for later development of this new type of MR-conditional pneumatic motor. Detailed accuracy test in various operating conditions are also investigated in detail.

## MATERIALS AND METHODS

### *Stepper Motor Assembly and Components*

Figure 1 shows the assembly design of the pneumatic stepper motor consisting of six key components: planetary gearbox, supporting structure, connecting bushes, cylinders, shafts and cranks. To ensure the MR safety and compatibility, all the major components are made of non-magnetic material—acrylonitrile butadiene styrene (ABS), of which the friction coefficient is relatively small and as low as 0.080, referring to the ASTM D1894 test method. This promising mechanical property is guaranteed due to the high-impact resistance of ABS. An MR-conditional planetary gearbox (made by ABS, Tamiya, Inc., Shizuoka, Japan) was integrated to gear down the speed in order to elevate the output torque. The friction is further reduced by putting few amount of semisolid lubricant onto the gear so as to ensure the efficiency, reliability and durability of the system.

The two cylinders, cranks and supporting structure form the crank-link mechanism which provides the actuation in discrete steps. The pneumatic cylinders used in the motor prototype are LEGO® components (part number: x189c01). They guarantee robust linear actuation, and also have been tested and used in many high-precision and low-friction electromagnetically powered mechanisms (e.g., Ref. 2). Their high quality

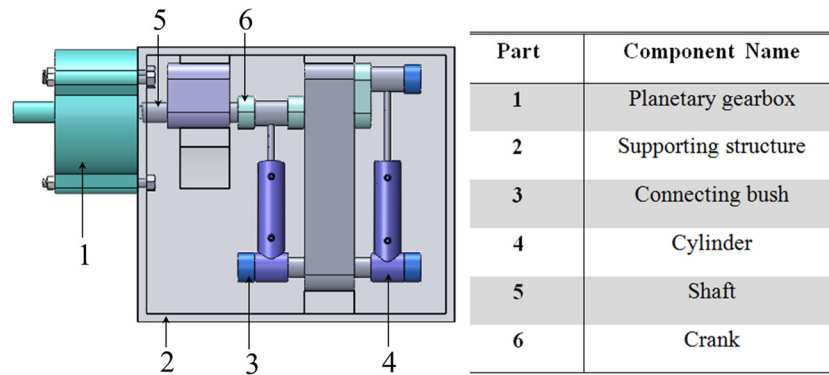


**FIGURE 1.** A 3-D assembly view of the stepper motor consisting of six major components, all of which are made of ABS.

control regarding the component dimension and surface smoothness is of great benefit to robust performance of our motor. No air leak was detected by the manometer before the assembly.<sup>24</sup> As a result, the air leakage phenomenon among the two chambers of the cylinders can be neglected.

#### Working Principle

Two cylinders are coupled along a rotating axis, between which the pressure difference provides the elemental driving force of the mechanism. Each cylinder has two ports supplied with pressured air in different time phase. The pressure difference is induced when either one of the chambers is pumped with air. This generates movement of the piston towards the opposite side at the lower pressure, in turn providing a torque about the rotation center. As a result, the actuation acts a pair of two stroke engines such that two pistons can extend and contract the stroke sin constantly 90° phase difference. Note that the second cylinder attachment is offset circumferentially by 90° from the first cylinder. This ensures that whenever one cylinder is at a critical motive point, the other cylinder is at a point allowing for exerting an effective force to resume the rotation. Figures 2a, 2b, 2c, and 2d illustrates a complete sequential motion of the proposed stepper motor. The motor home position (Fig. 2a) is defined where its right cylinder is at the critical movement position. The left cylinder and the right one are, respectively, extended and contracted simultaneously, thus generating angular movements about the rotating axis. This force drives the motor to rotate 90° as in Fig. 2b. Once both cylinders contract, they drive the motor to rotate another 90° (Fig. 2c). In the next phase of motion, the left cylinder keeps being contracted, while the right one is being extended; thereby causing the step motor reached to the position as shown in Fig. 2d. Both cylinders will then extend to return the home position (Fig. 2a). The stepper motor

operates in angular resolution of 90° acting as a single step size, throughout the sequential motion. The gearbox is integrated to reduce such a step size into a desired angle. For example, the use of 25:1 gearbox can minimize the step to 3.6°.

#### Theoretical Calculations

We hypothesize that dimensions of the cranks and cylinder are correlated to output torque of the stepper motor. Figure 2e shows the motor operating schematic diagram from side view. Force  $F_1$  denotes the extension force of the left cylinder, and  $F_2$  is the contraction force of the right cylinder. Then the force provided by each cylinder ( $F_1, F_2$ ) can be written as

$$F_i = P_i \cdot S (i = 1, 2), \quad (1)$$

where  $P$  is the pressure difference of two cylinder chambers of each cylinder, and  $S$  is a constant representing the effective area of the piston moved along inside the cylinder. Apart from static friction, we also realize the Coulomb and viscous friction can be likely induced during the motor motion; however, provided with the piston movement at a very low speed (<30 mm/s) in our application, the power dissipated on such frictions is extremely low<sup>11,22</sup> with respect to frictions caused by the other parts, e.g., the gear box. The friction between the cylinder and chambers is then neglected; hence,  $F_1$  and  $F_2$  are regarded as constant values during the operation, since both the air pressure and piston area are maintained at constant level during the motor operation.

Without loss of generality,  $F_1$  and  $F_2$  can be normalized in unit of 1 N in order to simplify the calculation of the motor configuration. Let the radius of cylinder tip trajectory be  $r$ , and the distance  $oo'$  between the crank axis and the pivot point of the cylinder be  $l$ . The angle between  $F_1$  and the normal direction can be achieved based on the triangle side formula below:

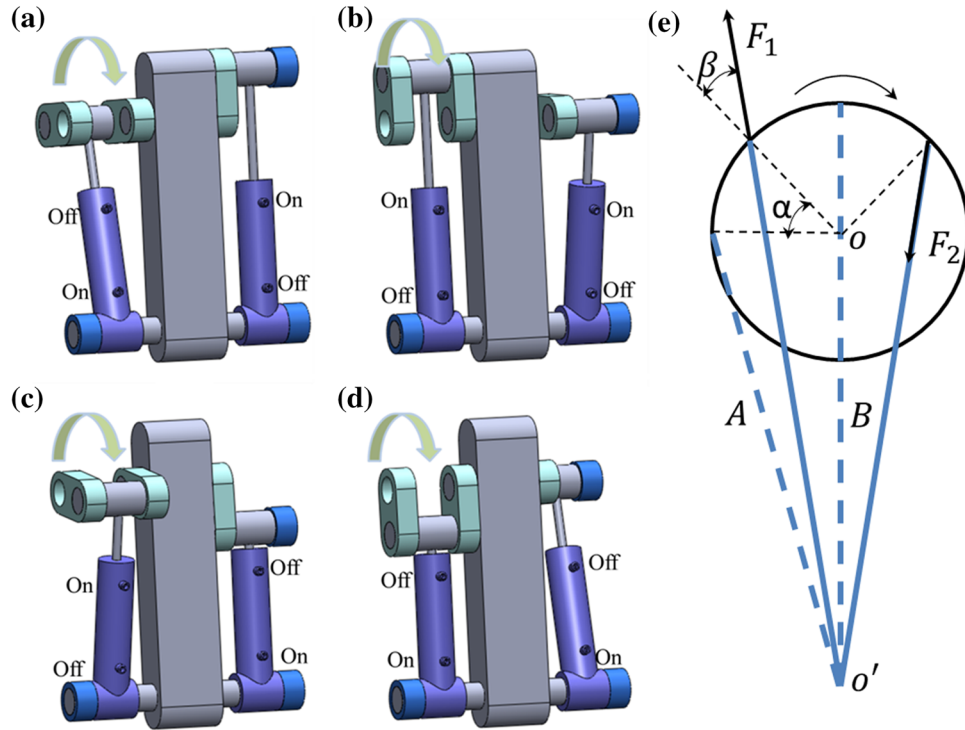


**FIGURE 2.** (a–d) Pneumatic control sequence for yielding one rotation cycle in 360°. Each sequential step is actuated by the pressured air flow regulated by closing (off) and opening (on) the corresponding pneumatic valves. The reverse of the step sequence yields rotation the other way around. (e) Schematic diagram showing the force components  $F_1$  and  $F_2$  coupling along the axis ( $o$ ) of rotation. The dashed blue line indicates the initial configurations of the two cylinders. After  $\alpha$ -degree rotation, the current two configurations are indicated by the solid blue lines. The axis  $o'$  denotes rotation axis of the cylinder base.

$$\sin \beta = \frac{l \sin(\alpha + 90)}{\sqrt{r^2 + l^2 - 2rl \cos(\alpha + 90)}} \quad (2)$$

Therefore, the output torque generated by cylinder  $A$  and  $B$  can be written as:

$$\begin{aligned} T_A &= \frac{F_1 r l \sin(\alpha + 90)}{\sqrt{r^2 + l^2 - 2rl \cos(\alpha + 90)}}, \\ T_B &= \frac{F_2 r l \sin(180 - \alpha)}{\sqrt{r^2 + l^2 - 2rl \cos(180 - \alpha)}} \end{aligned} \quad (3)$$

As a result, the output torque of the whole system is summarized by  $T_A$  and  $T_B$ :

$$T = T_A + T_B \quad (4)$$

Referred to Eqs. (1–4), the output torque is proportional to the pressure (st.  $T \propto \Delta P$ ). Increasing air pressure difference between two cylinders is an alternative to obtain the higher output torque in some cases. It is worth noting that the range of  $\alpha$  within a single step is always  $[0, 90^\circ]$  in one working step. Provided with the mechanical constraint that  $r$  is always constant, the system output torque with respect to  $\alpha$  and  $l$  can be obtained, of which the 2-D function is depicted as in Fig. 3a.

The output torque rises to its saturate level when the value of  $l$  increases further. Figure 3b shows the growth of output torque is significant only in a smaller value of  $l$ , at any angular configuration,  $\alpha$ . For instance, at  $\alpha = 45^\circ$ , the output torque is about to reach its upper bound (10.5 mN m) for  $l = 70$  mm. About 90% of maximum torque is already achieved with length  $l$  of 40 mm. It implies that system output torque will no longer improve obviously with an excessively long piston rod; in contrast, this will significantly increase the motor size in an unpractical way. The correlation between the output torque and the radius can be similarly obtained. The choice of motion radius is taken into consideration of two constraints: (1) radius  $r$  has to be smaller than separation  $l$ ; (2) the dimension of the whole system has to be minimized. Optimal value of  $l$  is found to be 40 mm and  $r$  is 8 mm for our design.

## RESULTS

Figure 4 illustrates an exemplary setup of MRI-guided intervention in the clinical environment, where the pneumatic actuation system is implemented in and connected between the MRI room and the control

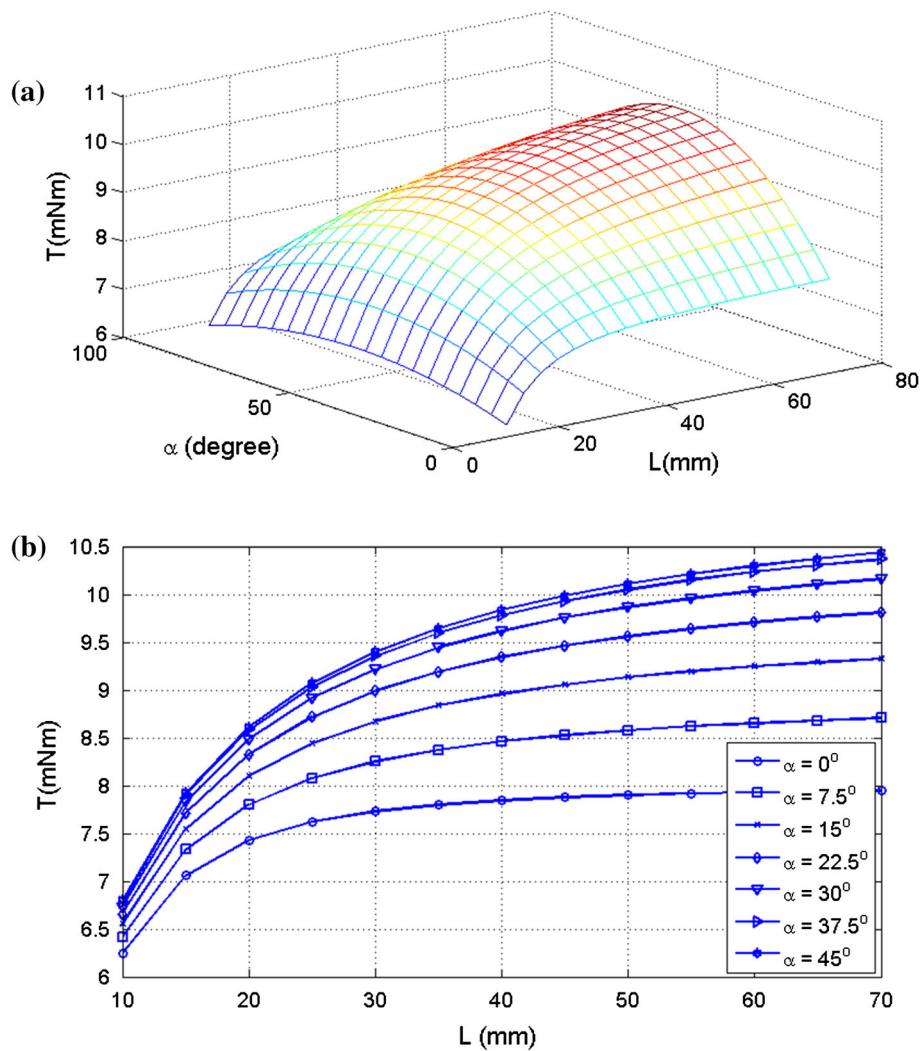


FIGURE 3. (a) Output torque denoting a 2-D function varying by angular displacement  $\alpha$  and separation  $l$  between two axes  $oo'$  (Fig. 2); (b) Output torque with respect to separation  $l$ .

room. In the MRI room, the system comprises the proposed pneumatic stepper motor, four MR-conditional piezoelectric valves (PS11111-B, Hoerbiger, Germany), piezoelectric driver, a 24 V battery power supply, and optical-electrical (O-E) converter (Fiber Optic Audio Link, CARL'S ELECTRONICS, USA), all of which are electromagnetically shielded in radio frequency faraday enclosure. Instead of using solenoid-operated valve, which would affect the homogeneity of the magnetic field and then deteriorate the MR image quality, the piezoelectric valve made of piezo-ceramic materials is adopted to regulate the input air pressure. In the control room, the control signal is transmitted via optical fibers from a data acquisition (DAQ) card (USB-6009, NI, USA) and a PC using an E-O converter. It is worth noting that the operation sequence of two ports in one cylinder has to be opposite; therefore, two sets of optical/fiber converters are

adopted to control two corresponding cylinders. An eight-meter pneumatic hose is used to channel the compressed air from the source to the four piezoelectric valves. The pressured air flow is regulated by the pneumatic valves, and conveyed through the four hoses connecting with the stepper motor. The air hoses connecting the piezoelectric valve and stepper motor are less than 1 meter in order to minimize the actuation delay.

#### Motor Torque Characteristics

Output torque is one of the primary standards to evaluate the actuation performance of a stepper motor,<sup>26,28</sup> which also determines the overall dynamic response of a robotic structure. As shown in Fig. 5, the output torque of our motor with respect to various levels of speed and input air pressure is investigated.

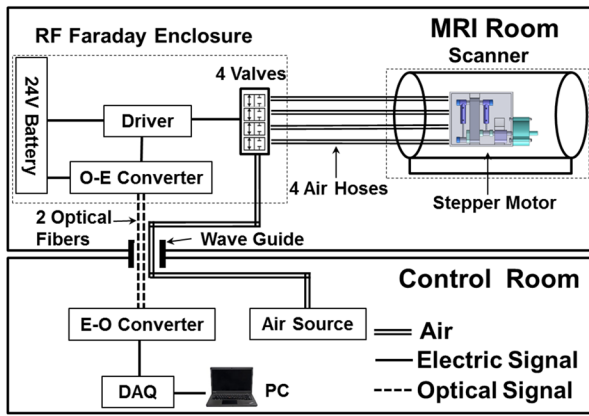


FIGURE 4. An overview of the presented motor and its electronic driver in MRI scanner room and control room.

The overall output torques are higher than that of the three stepper motors aforementioned, relative to the same air pressures. The maximum torque is approximately 800 mN m under mostly tolerated input air pressure at 80 psi. Each data line in Fig. 5 comprises seven data points which were experimentally obtained for validation of the motor performance. The torques were measured by a 1:1 pulley system<sup>3</sup> coupling with the motor. This system enables the motor to hoist a load varied by the numbers of identical mass (2.5 g). The evenly separated data lines at constantly increasing levels of pressure demonstrate that, the torque–pressure behaviors within a certain reasonable range of speed (0.5–4 step/s) are consistent with the working principal theoretically deduced in “Materials and Methods” section. Such linear behaviors may not be hold inherently in many complicated pneumatic actuation systems. Air supply is usually available in imaging room through the medical piped gas system in hospital.<sup>25</sup> The system provides clean air and its pressure is maintained as high at 55 psi, larger than the baseline pressure (30 psi) for operating the motor.

Similar to their motor characteristics, the decline of torque with increasing speed due to a low-pass filter effect<sup>28</sup> can be observed within the range of speed given in Fig. 5. It is because the compressible air is driven into the hose with higher speed, thus causing the damping of the pressure waves inside the hose. This torque performance is comparable to *PneuStep* which was adopted in a robotic system to perform transperineal percutaneous needle access for prostate brachytherapy under MRI guidance, of which the maximum torque is about 650 mN m with an input pressure of 120 psi. Furthermore, our proposed motor operates with much stronger output torque of 230 mN m, but at a normal air pressure of 30 psi only. The allowable torque of our presented motor is larger than the commercial MR-conditional piezoelectric motor, Shinsei USR-30, with its maximum output torque of 50 mN m. As compared,

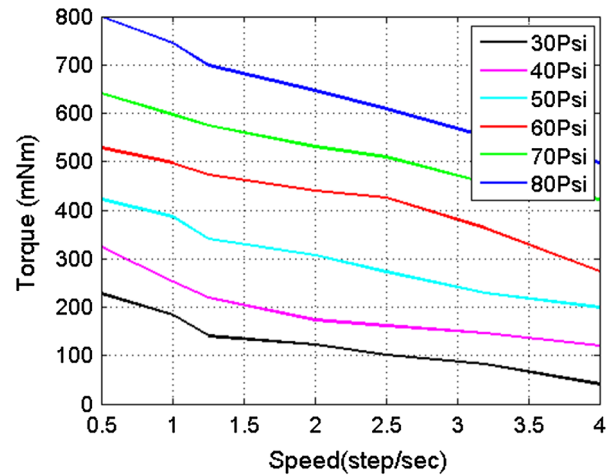


FIGURE 5. Output torque varied with motor speed regulated by the operating frequency of the pneumatic valves. Six levels of air pressure were tested.

our motor allows for higher flexibility in designing a robotic instrument through the adjustment of input air pressure, so as to fulfill various requirements for wider range of surgical applications.

Figure 6 shows the proportional correlation between output torque and input air pressure at seven levels of operating speed. The linear regression is applied to describe this correlation. It results in  $R^2$  values lightly ranging from 0.9873 to 0.9962. The resultant slopes of regression lines are estimated from 11.39 to 9.31. This coincides with the theoretical model denoted in Eqs. (1–4) that the output torque is always proportional to input air pressure. Theoretical value of the constant gradient can be deduced and calculated as nearly  $\approx 16$ . Such difference from this theoretical value is due to the energy power loss of any pneumatic driving approach, in which the energy transfer is mainly conducted by air movement from the pressured air source to the motor. The ideal and realistic output torque can be then expressed as:

$$T_1^I = 16P_1 + C_I, \quad T_1^R = 11.168P_1 + C_R, \quad (6)$$

Where  $C_I$  and  $C_R$  are the  $y$ -intercept constants of their corresponding linear regressions at speed  $v = 0.5$  steps/s, and  $P_1$  denotes the air pressure supplied at time  $t_1$ . Applying a certain amount of pressure change, the efficiency of power transfer from time  $t_1$  to  $t_2$  can be obtained as:

$$\eta = \frac{T_2^R \cdot v - T_1^R \cdot v}{T_2^I \cdot v - T_1^I \cdot v} = \frac{11.168(P_2 - P_1)}{16(P_2 - P_1)} = 69.8\% \quad (7)$$

This experimental efficiency outperforms many sophisticated pneumatic actuators, their power efficiency can only be maintained around 20–30% in

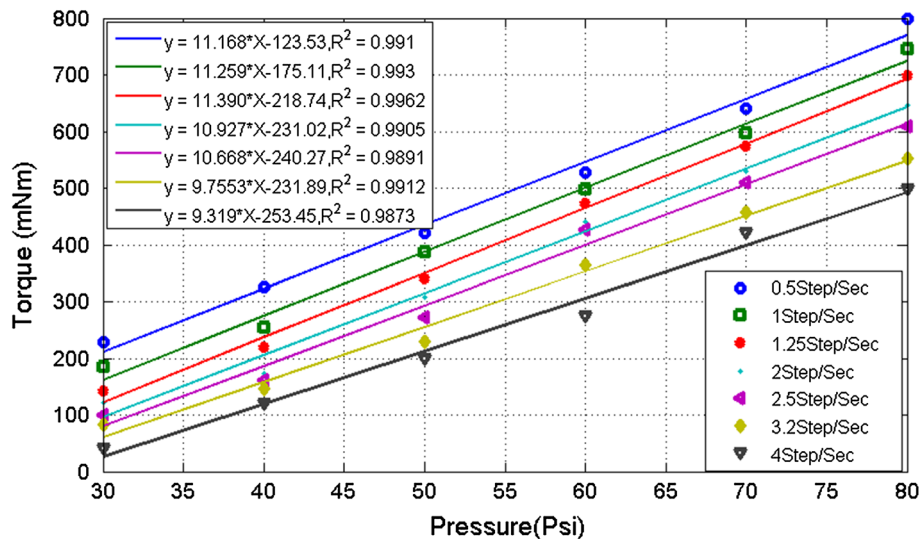


**FIGURE 6.** Output torque with respect to air pressure ranging from 30 to 80 psi. Each linear regression applied to six sampling points in the experiment.

many cases.<sup>5,19</sup> Simple design of our motor comprises small number of pneumatic components attributes the effective power transfer generally above 50%.

#### Motor Accuracy Analysis

The motor accuracy was tested under different control specifications, namely, angular speed, gear ratio and target rotation angle, with constant air pressure (=30 psi) applied. To measure the accuracy of the stepper motor, the motor shaft was coupled with an optical encoder (E6B2-CWZ3E, OMRON, USA) that is capable of measuring rotation angle in the resolution of 0.35°. Masamune and co-authors,<sup>26</sup> the frontier developers of MRI-compatible pneumatic stepper motor, who suggested a testing protocol to divide one revolution into three target angles for accuracy analysis. Five divisions are applied in our case so as to achieve a finer measurement; hence, each target angle occupies 72°. In order to minimize the measurement error, each data point in Figs. 7a, 7b is a mean of error values sampled by 5 times per trial. Figure 7a shows the correlation between the motor accuracy and the target angle. The motor operating speed measured in unit of steps per second is controlled by regulating operating frequency of the pneumatic valves. Three levels of operating speed are specifically selected for applications involving relatively slow and delicate robotic manipulation of needle insertion and catheterization. The motor was test repeatedly five times at the same condition; thereby, to find out the statistical significance, a two-way analysis of variance (ANOVA)<sup>14</sup> test is applied to all position errors obtained at different levels of speed and target angle. Both column and row  $p$ -values (<0.0002) far below a preset threshold level

(=0.01). This small  $p$  value is evidence showing five-time sampling is sufficient and the total number of samples is already lack of reproducibility.<sup>15</sup> This demonstrates both the target angle and operating speed are the independent factors significantly yielding the rise of the angular displacement error. Furthermore, it is also observed that the accuracy of the presented motor is higher than that developed by Masamune *et al.* Figure 7b shows the accuracy in the similar testing conditions, but the speed is altered with the use of three different gear ratios (25:1, 16:1, and 5:1). It is obvious that the larger gear ratio (the smaller step size), the smaller rotation error can be achieved. This error pattern is also similar to the pattern found in Fig. 7a of which the motor operation speed level is varied based on the pneumatic valve frequency. Both error patterns demonstrate an inverse relationship between the position error and the target angle; thereby, lower operating speed and larger gear ratio, both are the manners to guarantee the higher rotation accuracy. Wide range of gearbox with various gear ratios can be adopted in consideration of any specific clinical application. Regulating frequency of the pneumatic valve would be an effective alternative to adjust the speed of instrument manipulation. Real-time adjustment of gear ratio may yield a flexible change of output torque; however, the force-based control is required, and it is hitherto not an attractive feature even in sophisticate surgical robotic systems (e.g., Intuitive da Vinci® System). Those systems deal with dynamic surgical scenarios just using position-based controller associated with motor encoders. In contrast, direct control of rotary position is the inherent capability of stepper motor that can strictly prescribe the instrument displacement by just commanding a certain number of discrete steps.

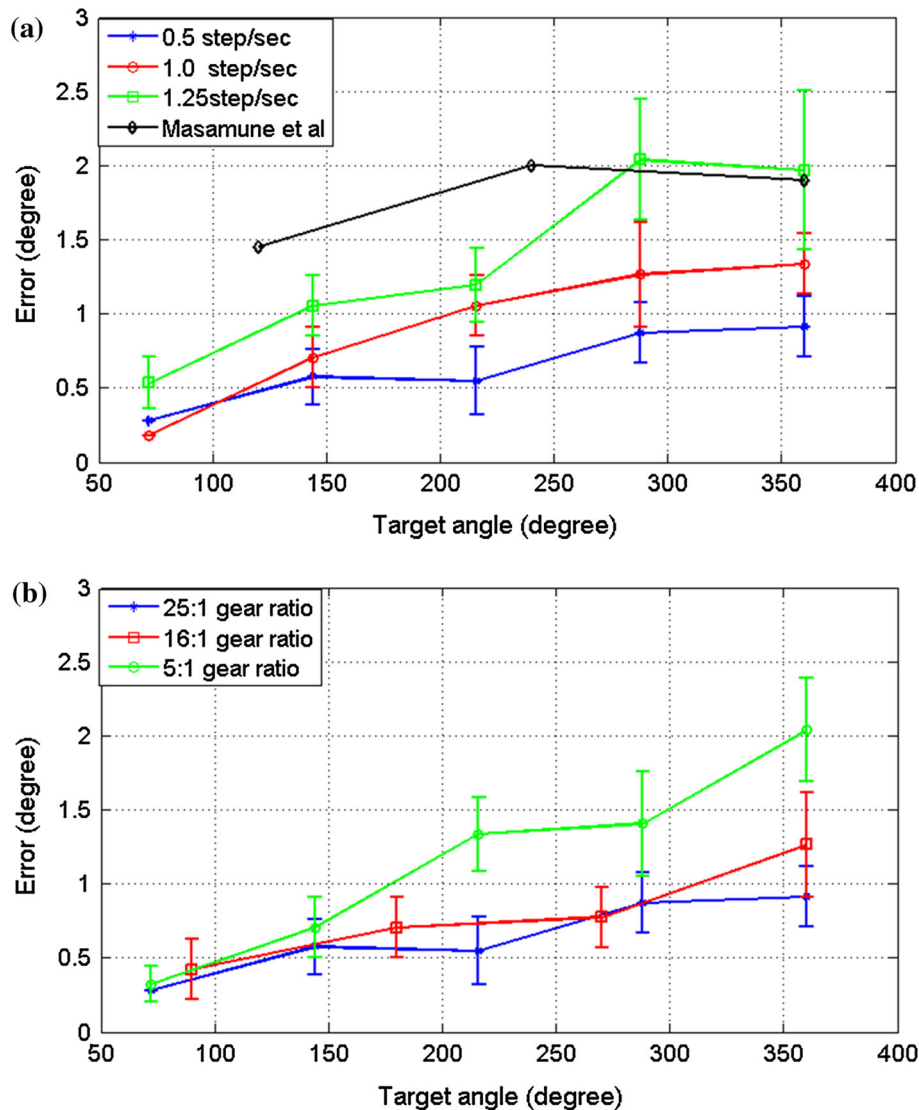


**FIGURE 7.** (a) Angular errors with respect to target angles from 72° to 360°. Each data point represents the mean of five sampling values at the same testing condition. Error induced by the motor proposed by Masamune and co-authors<sup>26</sup> is included for comparison; (b) Angular errors at three different gear ratios.

The comparative study of the motor physical parameters between our presented motor and the existing three motors is depicted in Fig. 8. Each stepper motor is ranked based on five evaluation standards. Our presented motor provides the largest torque, but also occupies the most volumetric size. The step size of our motor is similar to those developed by Stoianovici *et al.* and Masamune *et al.*; however, we demonstrate that our motor can flexibly adjust the step size with gearbox in different gear ratios in order to satisfy various operating requirements. The power of our presented motor is similar to that of one designed by Stoianovici *et al.*, both of them far outweigh the other two motors. Only few components are involved in our design. The simplicity of working principle is

considered as a very impressive characteristic for ease of the reliable implementation in many real practices.

#### *Compliance to MRI Environment*

Figure 9a shows the experimental setup in the MRI room aiming to quantify the compliance of the present motor with the MRI environment by measuring the SNR and the maximum width of image artifacts generated by the motor.<sup>27,33</sup> The ASTM F2119 standard<sup>1</sup> was used to quantify the size of the image artifacts surrounding the presented motor. Image artifact is defined by 30% changes of the pixel intensity in the MR image before and after the introduction of the tested motor.<sup>1</sup> No obvious image artifact can be



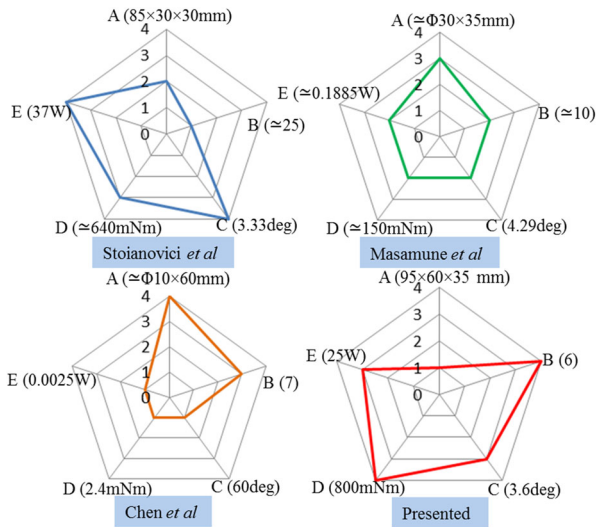


**FIGURE 8. Comparison among five evaluation standards. Note that rank 4 denotes the best in its corresponding standard. The larger the size of pentagon, the better is the overall performance in terms of A: motor dimension, B: number of components, C: step size, D: motor output torque, E: power.**

observed apart from the motor components themselves.

For the SNR test, the motor was put in a container filled with  $\text{CuSO}_4$  solution and imaged at the isocenter of the scanner, where induced with the strongest magnetic field. The turbo spin echo (TSE) and gradient echo (GRE) sequences were adopted to obtain the MR images. The scanning parameters are listed in Table 1. The representative MR images obtained within the 3T GE scanner (GE SignaHDx, GE Healthcare, Milwaukee, WI, USA) under two different sequences and motor operation conditions (OFF/ON) can be seen in Fig. 9b. The SNR value is calculated<sup>8</sup> as follows:

$$SNR = \frac{I_{\text{center}}}{SD_{\text{corner}}}$$

where  $I_{\text{center}}$  is the mean of the intensity values within the  $40 \times 40$  pixel region located at the image center, and  $SD_{\text{corner}}$  is the standard deviation of the intensity values within the  $40 \times 40$  pixel region at the image corner. Note that the FOV dividing the in-plane resolution gives the base matrix size, whereas the matrix size is 512 according to Table 1 and therefore  $40 \times 40$  pixel region is  $16 \times 16 \text{ mm}^2$  in the real dimension. The SNR analysis was performed similarly to evaluation of other MR-conditional devices.<sup>8,30</sup> Figure 10 shows the SNR generated by the stepper motor under three conditions, when the motor is: (1) not in the MR scanner; (2) is at rest but with electronics powered; (3) in motion. It is worth noting that the SNR value is calculated based on the images obtained within the 3T Siemens MRI scanner (MAGNETOM Skyra, Siemens Medical Solutions, Erlangen, Germany). The first condition is selected as

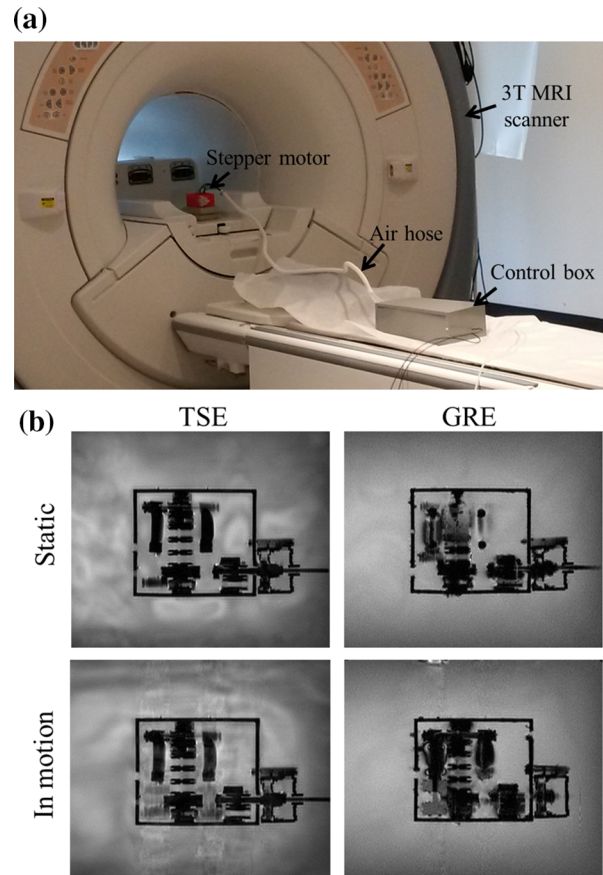


**FIGURE 9. (a) System setup in the MR room. The control box is connected with the computer in control room through two optical fibers; (b) TSE and GRE images of the experimental setup.**

the control experiment. The moving motor causes the most reduction relative to the control; however, it still reduces  $\approx 2.35\%$  that is within an acceptable range.<sup>8</sup>

## DISCUSSION

This paper presents a design of pneumatic stepper motor with the relatively simple working mechanism. The motor output torque performance, rotation accuracy and repeatability, pneumatic actuation parameters as well as its MRI compatibility were tested and investigated in detail. Compared to the current advanced pneumatic motors compatible with MRI,<sup>7,26,28</sup> our simple-designed motor comprises far fewer numbers (= 6) of components such that only a pair of two-stroke engines is required to generate the stepper movement, instead of using gear mechanism. The primary merit is that, in a reasonable size, the motor offers not just the large range of output torques ( $< 800 \text{ mN m}$ ), but also ensures high accuracy for robotic actuation. These act as important features for minimally invasive surgery (MIS). Detailed assessment scheme has also been

**TABLE 1. Scanning parameters for the MR compatibility evaluation.**

Imaging sequence	FOV (mm)	TE (ms)	TR (ms)	FA (°)	Resolution	Bandwidth (Hz/pixel)
TSE	200	99.68	3000	90	0.3906 × 0.3906 × 4	127.07
GRE	200	11	500	18	0.3906 × 0.3906 × 4	127.07

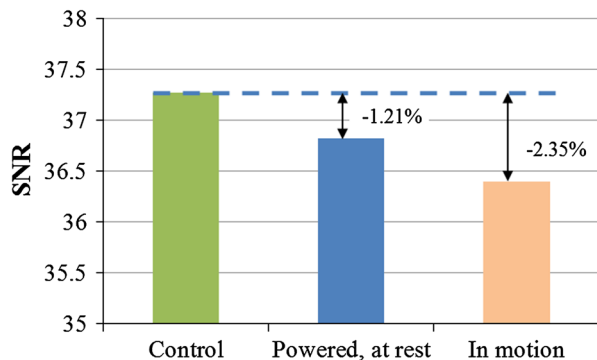


**FIGURE 10. SNR generated on GRE images under 3 different conditions. Control condition** obtained when the motor is not placed in the scanner. This serves as the baseline for comparison; **Powered (at rest) condition** realized by sending the operation signal to the control box while the air source pressure is set to zero. This ensures the motor not being actuated; **In-Motion condition** obtained when the motor operates normally.

proposed which serves as a benchmark for the future design of MR-conditional pneumatic motor.

The proposed motor was repeatedly operated at various target angles, with respect to several operating conditions: air pressure, gear ratio and pneumatic valve frequency, of which the optimal combination for higher accuracy was also investigated. With the design simplicity of this motor, the investigated performances are found to be consistent with the expected mathematic model deduced from its simple working principle. In terms of the image quality, we also prove that the proposed motor does not generate any observable artifact on the MR images, and it causes minimal SNR reduction during the motor operation under the MRI. All these merits demonstrate its high clinical potential for application in MR image-guided and robot-assisted MIS. Potential applications include treatments, not just demanding for high surgical precision, but also taking much clinical advantage of monitoring both morphological and pathological changes intra-operatively under the MRI. Development of a MR-conditional robot system for transperineal percutaneous needle intervention would be the easiest implementation with our motor. Through the rotary-to-linear mechanism, our motor will enable robust and accurate needle insertion to deliver the seeds at the prostate target. Our motor operation guarantees little to no distortion of the intra-operative MR images. For other MR-guided interventions, such as catheter-based cardiac EP therapy, micro-neurosurgery and stereotaxy, which involve relatively

complicated manipulation in higher degree of freedom (DoF),<sup>17</sup> several motors will have to be integrated in a rather confined structural space; therefore, our ongoing work focuses on miniaturization of the motor design by exploiting advances of high-precision 3D printing, so that the motion accuracy will also be improved. It is also expected that coupling different fixed gear ratios with particular motors can provide specific range of speed and output torque on each robotic DoF, thus ensuring safe intervention. In the future work, we will integrate these motors into a robotic instrument motorized with multiple DoFs. The overall performance will be evaluated under MRI by measuring the position of its instrument tip with the use of our MRI-conditional active tracking coil system.<sup>23</sup>

#### ACKNOWLEDGMENTS

This work was supported by National Institutes of Health (NIH) U41-RR019703, Dr. Richard J. Schlesinger Grant, and The Croucher Foundation Fellowship.

#### CONFLICT OF INTEREST

None to declare.

#### FINANCIAL DISCLOSURE

None to declare.

#### REFERENCES

- <sup>1</sup>ASTM. F2119 Standard Test Method for Evaluation of MR Image Artifacts from Passive Implants. <http://www.astm.org/Standards/F2119.htm>, 2013. Accessed 28 June 2013.
- <sup>2</sup>Bergeles, C., P. Vartholomeos, L. Qin, and P. E. Dupont. Closed-loop commutation control of an MRI-powered robot actuator. In: 2013 IEEE International Conference on Robotics and Automation (ICRA), 2013, pp. 698–703.
- <sup>3</sup>Bhavikatti, S., and K. Rajashekarappa. Engineering Mechanics. New Delhi: New Age International, 1994.
- <sup>4</sup>Briggs, R. W., I. Dy-Liacco, M. P. Malcolm, H. Lee, K. K. Peck, K. S. Gopinath, *et al.* A pneumatic vibrotactile stimulation device for fMRI. *Magn. Reson. Med.* 51:640–643, 2004.
- <sup>5</sup>Cai, M., K. Kawashima, and T. Kagawa. Power assessment of flowing compressed air. *J. Fluids Eng.* 128:402–405, 2006.

- <sup>6</sup>Chen, Y., J. Ge, K.-W. Kwok, K. R. Nilsson, M. Fok, and T. T. Zion. MRI-conditional catheter sensor for contact force and temperature monitoring during cardiac electrophysiological procedures. *J. Cardiovasc. Magn. Reson.* 16:P150, 2014.
- <sup>7</sup>Chen, Y., C. D. Mershon, and Z. T. H. Tse. A 10-mm MR-conditional unidirectional pneumatic stepper motor. In: *IEEE/ASME Transactions on Mechatronics*, Vol. 13, 2014, pp. 1–7.
- <sup>8</sup>Chinzei, K., R. Kikinis, and F. A. Jolesz, MR compatibility of mechatronic devices: design criteria. In: *Proceedings of Medical Image Computing and Computer-Assisted Intervention, Miccai'99*, Vol. 1679, Jan 1999, pp. 1020–1030.
- <sup>9</sup>Fischer, G. S., I. Iordachita, C. Csoma, J. Tokuda, S. P. DiMaio, C. M. Tempny, *et al.* MRI-compatible pneumatic robot for transperineal prostate needle placement. In: *IEEE/ASME Transactions on Mechatronics*, Vol. 13, 2008, pp. 295–305.
- <sup>10</sup>Gassert, R., A. Yamamoto, D. Chapuis, L. Dovat, H. Bleuler, and E. Burdet. Actuation methods for applications in MR environments. *Concepts Magn. Reson. Part B* 29B:191–209, 2006.
- <sup>11</sup>Ge, Y., L. Chen, F. Sun, and C. Wu. Thermodynamic simulation of performance of an Otto cycle with heat transfer and variable specific heats of working fluid. *Int. J. Therm. Sci.* 44:506–511, 2005.
- <sup>12</sup>Hall, W. A., and C. L. Truwit. Intraoperative MR-guided neurosurgery. *J. Magn. Reson. Imaging* 27:368–375, 2008.
- <sup>13</sup>Hetts, S., M. Saeed, A. Martin, L. Evans, A. Bernhardt, V. Malba, *et al.* Endovascular catheter for magnetic navigation under MR imaging guidance: evaluation of safety in vivo at 1.5 T. *Am. J. Neuroradiol.* 34:2083–2091, 2013.
- <sup>14</sup>Hogg, R. V., and J. Ledolter. *Engineering Statistics*, Vol. 358. New York: MacMillan, 1987.
- <sup>15</sup>Johnson, V. E. Revised standards for statistical evidence. *Proc. Natl. Acad. Sci.* 110:19313–19317, 2013.
- <sup>16</sup>Kwok, K.-W., Y. Chen, T. C. Chau, W. Luk, K. R. Nilsson, E. J. Schmidt, *et al.* MRI-based visual and haptic catheter feedback: simulating a novel system's contribution to efficient and safe MRI-guided cardiac electrophysiology procedures. *J. Cardiovasc. Magn. Reson.* 16:O50, 2014.
- <sup>17</sup>Kwok, K.-W., K. H. Tsoi, V. Vitiello, J. Clark, G. C. Chow, W. Luk, *et al.* Dimensionality reduction in controlling articulated snake robot for endoscopy under dynamic active constraints. In: *IEEE Transactions on Robotics*, Vol. 29, 2013, pp. 15–31.
- <sup>18</sup>Lieberman, L., N. Bracero, E. Morris, C. Thornton, and D. D. Dershaw. MRI-guided 9-gauge vacuum-assisted breast biopsy: initial clinical experience. *AJR Am. J. Roentgenol.* 185:183–193, 2005.
- <sup>19</sup>Maolin, C. and T. Kagawa, Energy consumption assessment of pneumatic actuating systems including compressor. In: *Proceeding of International Conference on Compressors and their Systems*, 2001, pp. 381–390.
- <sup>20</sup>Masamune, K., E. Kobayashi, Y. Masutani, M. Suzuki, T. Dohi, H. Iseki, *et al.* Development of an MRI-compatible needle insertion manipulator for stereotactic neurosurgery. *Comput. Aided Surg.* 1:242–248, 1995.
- <sup>21</sup>McRobbie, D. W., E. A. Moore, M. J. Graves, and M. R. Prince. *MRI from Picture to Proton*. Cambridge: Cambridge University Press, 2006.
- <sup>22</sup>Ozsoysal, O. A. Heat loss as a percentage of fuel's energy in air standard Otto and Diesel cycles. *Energy Convers. Manag.* 47:1051–1062, 2006.
- <sup>23</sup>Qin, L., E. J. Schmidt, Z. T. H. Tse, J. Santos, W. S. Hoge, C. Tempny-Afdhal, *et al.* Prospective motion correction using tracking coils. *Magn. Reson. Med.* 69:749–759, 2013.
- <sup>24</sup>Richer, E., and Y. Hurmuzlu. A high performance pneumatic force actuator system: part I—nonlinear mathematical model. *J. Dyn. Syst. Meas. Contr.* 122:416–425, 2000.
- <sup>25</sup>Robinson, J. An appraisal of piped medical gas systems. *Br. J. Hosp. Med.* 28:160, 1982.
- <sup>26</sup>Sajima, H., H. Kamiuchi, K. Kuwana, T. Dohi, and K. Masamune. MR-safe pneumatic rotation stepping actuator. *J. Robot. Mechatron.* 24:820–827, 2012.
- <sup>27</sup>Stoianovici, D. Multi-imager compatible actuation principles in surgical robotics. *Int. J. Med. Robot. Comput. Assist. Surg.* 1:86–100, 2005.
- <sup>28</sup>Stoianovici, D., A. Patriciu, D. Petrisor, D. Mazilu, and L. Kavoussi. A new type of motor: pneumatic step motor. In: *IEEE/ASME Transactions on Mechatronics*, Vol. 12, Feb 2007, pp. 98–106.
- <sup>29</sup>Tse, Z. T. H., H. Elhawary, M. Rea, B. Davies, I. Young, and M. Lamperth. Haptic needle unit for MR-guided biopsy and its control. In: *IEEE/ASME Transactions on Mechatronics*, Vol. 17, Feb 2012, pp. 183–187.
- <sup>30</sup>Tse, Z. T. H., H. Elhawary, A. Zivanovic, M. Rea, M. Paley, G. Bydder, *et al.* A 3-DOF MR-compatible device for magic angle related in vivo experiments. In: *IEEE-ASME Transactions on Mechatronics*, Vol. 13, Jun 2008, pp. 316–324.
- <sup>31</sup>Vartholomeos, P., C. Bergeles, L. Qin, and P. E. Dupont. An MRI-powered and controlled actuator technology for tetherless robotic interventions. *Int. J. Robot. Res.* 32:1536–1552, 2013.
- <sup>32</sup>Wang, Y., H. Su, K. Harrington, and G. Fischer. Sliding mode control of piezoelectric valve regulated pneumatic actuator for MRI-compatible robotic intervention. In: *ASME Dynamic Systems and Control Conference-DSCC*, 2010.
- <sup>33</sup>Yu, N., R. Gassert, and R. Riener. Mutual interferences and design principles for mechatronic devices in magnetic resonance imaging. *Int. J. Comput. Assist. Radiol. Surg.* 6:473–488, 2011.